

中国激光

基于双振镜激光扫描的玻璃纤维复合板直壁孔制造

张聘³, 乔亚庆^{1*}, 苏晓慧¹, 高辉^{1,2}, 熊伟^{1,2}, 邓磊敏^{1,2}

¹华中科技大学武汉光电国家研究中心, 湖北 武汉 430074;

²湖北光谷实验室, 湖北 武汉 430074;

³航空工业济南特种结构研究所高性能电磁窗航空科技重点实验室, 山东 济南 250023

摘要 为改善玻璃纤维复合材料制孔的精度和质量, 本文提出了一种双振镜激光扫描加工方法。双振镜激光扫描加工系统共包括4片可偏转反射镜, 4片反射镜协同运动可以实现对扫描激光的四轴(x, y, α, β)控制, 其中 x 和 y 为激光焦点在二维平面的位置, α 和 β 为扫描激光的入射角度。基于双振镜激光扫描加工系统开展了玻璃纤维复合材料的制孔实验, 通过调节激光入射角度和激光扫描策略, 在厚度为3.6 mm的玻璃纤维复合材料板上加工了侧壁完全垂直的孔, 孔直径可达10 mm, 热影响区宽度小于10 μm , 侧壁表面粗糙度小于2 μm , 没有发现材料分层和纤维拔出等缺陷。

关键词 激光技术; 激光钻孔; 四轴激光扫描; 玻璃纤维复合材料; 飞秒激光

中图分类号 TN05

文献标志码 A

DOI: 10.3788/CJL230763

1 引言

玻璃纤维复合材料具有耐磨、耐蚀、高比强度和高断裂韧性等特点, 已被广泛应用于航空航天、汽车、造船和化工等领域^[1-2]。然而, 玻璃纤维复合材料的结构特殊性导致其加工(尤其是制备高质量的孔结构^[3-4])异常困难。在机械制孔过程中, 钻头与材料之间的作用力会使材料出现分层、纤维拉出等缺陷, 影响加工质量^[5-8]; 在水射流钻孔过程中, 射流与材料之间同样也存在力的作用, 无法避免上述缺陷^[9-10], 同时, 纤维复合材料的吸湿性也会进一步导致其分层^[11-12]。

激光加工是一种非接触式加工方法。激光加工时激光与材料之间不存在相互作用力^[13-14], 可以避免上述加工缺陷, 是玻璃纤维复合材料的有效制孔方法^[15-16]。激光打孔的常见方式有激光冲孔、激光扫描制孔和激光旋切制孔^[17-18]。激光冲孔是用聚焦激光始终烧蚀材料的同一个位置, 直至材料被烧穿, 这种打孔方法只适用于加工直径较小的圆孔^[19-20]。在激光扫描制孔过程中, 激光焦点可以在扫描振镜的带动下在材料上绘制任意图形, 加工出不同形状的孔, 同时孔直径的大小也不受限制^[21-22]。然而, 激光冲孔和激光扫描制孔均无法调节孔侧壁的锥度, 自带锥角的聚焦激光只能加工人口大、出口小的正锥孔^[23-24]。激光旋切制孔通过旋转的楔形棱镜和道威棱镜的组合调节聚焦激光的倾斜角度, 可以避免孔侧壁对入射激光的遮挡, 进

而消除侧壁锥度^[25-26]。但是由于光学结构的限制, 激光旋切技术仅能加工圆孔, 且孔直径通常不超过1 mm^[27-28]。五轴激光加工系统也可以消除侧壁锥度, 实现直壁孔的加工^[29-30]。然而目前的五轴加工系统, 如 Scanlab 公司的 precSYS 微加工系统^[31]以及 Arges 公司的 Precession Elephant 2^[32], 均是面向微孔制造研发的, 加工幅面的最大直径分别为5 mm 和 3 mm, 无法加工直径更大的孔。并且上述加工系统使用的光学元件数量众多、结构复杂、成本较高, 难以实现大范围的工业应用。

激光冲孔和激光扫描制孔对激光控制的灵活性较差, 孔的侧壁锥度难以消除。激光旋切制孔和五轴激光制孔可以消除侧壁锥度, 但是加工范围有限。针对上述局限, 笔者提出了一种基于双振镜的四轴激光扫描加工技术, 通过建立激光焦点四轴坐标与振镜反射镜偏转角的对应关系实现四轴激光扫描; 之后基于双振镜激光扫描加工系统开展了玻璃纤维复合材料制孔实验, 探究了激光扫描策略和激光入射角度对孔侧壁锥度的影响。此外, 通过调节激光入射角结合边缘补偿扫描方法消除了侧壁锥度, 实现了直壁圆孔的加工, 孔的直径为10 mm, 孔入口和出口的几何尺寸完全一致, 热影响区宽度小于10 μm , 侧壁表面粗糙度小于2 μm , 没有发现材料分层和纤维拔出等缺陷。笔者提出的四轴激光制孔方法提升了激光运动的灵活性, 增大了四轴激光的加工范围, 提高了玻璃纤维复合材料的制孔精度和质量。

收稿日期: 2023-04-25; 修回日期: 2023-06-03; 录用日期: 2023-06-21; 网络首发日期: 2023-07-04

通信作者: *yaqiao@hust.edu.cn

2 双振镜激光扫描法

双振镜激光扫描法的工作原理如图 1 所示。振镜 1 中的两片反射镜为 G_1 和 G_2 , 振镜 2 中的两片反射镜为 G_3 和 G_4 。振镜 1 的出光口与振镜 2 的入光口同心, 激光从 O_1 点开始入射到加工系统中, 依次经 G_1 、 G_2 、 G_3 和 G_4 反射后再由 F-theta 镜聚焦到焦平面上, 聚焦激光点 O_1 的四轴坐标(x, y, α, β)由 4 片振镜的偏转角 $\theta_1, \theta_2, \theta_3$ 和 θ_4 控制, 其中 x 和 y 是聚焦激光在焦平面上的位置坐标, α 是聚焦激光束在 $X-Z$ 平面上的投影与 Z 轴之间的夹角, β 是聚焦激光束在 $Y-Z$ 平面上的投影与 Z 轴之间的夹角。

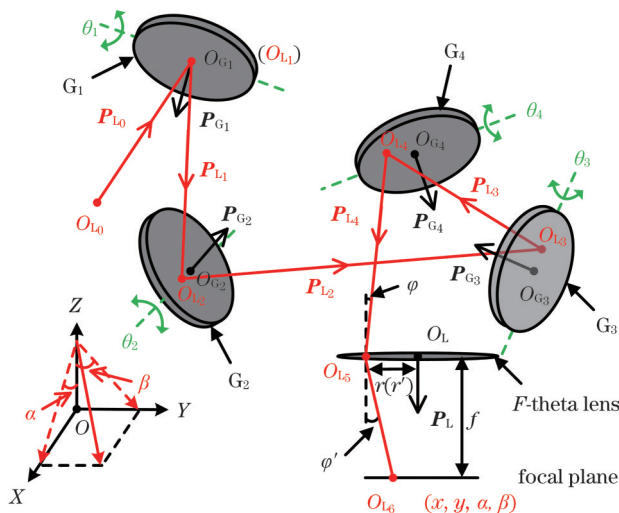


图 1 双振镜激光扫描法原理示意图

Fig. 1 Schematic diagram of the principle of dual galvanometer laser scanning method

双振镜激光扫描法中的激光传输路径如图 1 所示。入射激光的起点为 $O_{L_0}(x_{O_{L_0}}, y_{O_{L_0}}, z_{O_{L_0}})$, 激光传输的方向 P_{L_0} 可以表示为

$$P_{L_0} = (x_{P_{L_0}}, y_{P_{L_0}}, z_{P_{L_0}}) \quad (1)$$

双振镜中的 4 片反射镜(G_1, G_2, G_3, G_4)依次摆放在光路中, 各反射面的中心点坐标可以表示为

$$\begin{cases} O_{G_1}: (x_{O_{G_1}}, y_{O_{G_1}}, z_{O_{G_1}}) \\ O_{G_2}: (x_{O_{G_2}}, y_{O_{G_2}}, z_{O_{G_2}}) \\ O_{G_3}: (x_{O_{G_3}}, y_{O_{G_3}}, z_{O_{G_3}}) \\ O_{G_4}: (x_{O_{G_4}}, y_{O_{G_4}}, z_{O_{G_4}}) \end{cases} \quad (2)$$

各反射镜的法线方向可以表示为

$$\begin{cases} P_{G_1} = [0, -\cos(45^\circ + \theta_1), \sin(45^\circ + \theta_1)] \\ P_{G_2} = [\sin(45^\circ + \theta_2), 0, -\cos(45^\circ + \theta_2)] \\ P_{G_3} = [\sin(45^\circ + \theta_3), -\cos(45^\circ + \theta_3), 0] \\ P_{G_4} = [0, -\cos(45^\circ + \theta_4), \sin(45^\circ + \theta_4)] \end{cases} \quad (3)$$

式中: $\theta_1, \theta_2, \theta_3$ 和 θ_4 分别是 4 片反射镜的偏转角度。式(3)中的向量均为单位向量, 本文后续使用的向量也均为单位向量。

焦距为 f 的 F-theta 镜放置在 $O_L(x_{O_L}, y_{O_L}, z_{O_L})$ 点处, 代表其光轴方向的向量 P_L 可以表示为

$$P_L = (x_{P_L}, y_{P_L}, z_{P_L}) \quad (4)$$

入射激光首先被 G_1 反射, 根据反射定律, 出射激光的方向 P_{L_1} 可以表示为

$$P_{L_1} = P_{L_0} - 2(P_{G_1} \cdot P_{L_0})P_{G_1} \quad (5)$$

根据射线方程可得

$$OO_{L_2} = OO_{L_1} + t_{OO_{L_2}}P_{L_1} \quad (6)$$

式中: $t_{OO_{L_2}}$ 为射线方程系数, 其取值范围为 $[0, +\infty)$ 。

由于 $O_{L_2}O_{G_2}$ 和 P_{G_2} 相互垂直, 因此可以得到以下关系式:

$$P_{G_2} \cdot O_{L_2}O_{G_2} = 0 \quad (7)$$

根据式(6)和式(7)可得

$$OO_{L_2} = OO_{L_1} + \frac{P_{G_2} \cdot O_{L_1}O_{G_2}}{P_{G_2} \cdot P_{L_1}}P_{L_1} \quad (8)$$

激光与 G_2 相交的点 $O_{L_2}(x_{O_{L_2}}, y_{O_{L_2}}, z_{O_{L_2}})$ 是 OO_{L_2} 的终点。同理, 可以依次得到激光与 G_3, G_4 和 F-theta 镜的交点为

$$\begin{cases} O_{L_3}: (x_{O_{L_3}}, y_{O_{L_3}}, z_{O_{L_3}}) \\ O_{L_4}: (x_{O_{L_4}}, y_{O_{L_4}}, z_{O_{L_4}}) \\ O_{L_5}: (x_{O_{L_5}}, y_{O_{L_5}}, z_{O_{L_5}}) \end{cases} \quad (9)$$

激光的传输方向可以表示为

$$\begin{cases} P_{L_2} = (x_{P_{L_2}}, y_{P_{L_2}}, z_{P_{L_2}}) \\ P_{L_3} = (x_{P_{L_3}}, y_{P_{L_3}}, z_{P_{L_3}}) \\ P_{L_4} = (x_{P_{L_4}}, y_{P_{L_4}}, z_{P_{L_4}}) \end{cases} \quad (10)$$

然后, 将 $O_{L_4}O_{L_5}$ 分别投影到 $X-Z$ 和 $Y-Z$ 平面, 如图 2 所示。

设 O_{L_5} 与 O_L 之间的距离为 r , 激光束与光轴之间的夹角为 φ , 则它们可以表示为

$$\begin{cases} r_x = x_{O_{L_5}} - x_{O_L} \\ \varphi_x = \arccos x_{P_{L_4}} \\ r_y = y_{O_{L_5}} - y_{O_L} \\ \varphi_y = \arccos y_{P_{L_4}} \end{cases} \quad (11)$$

为了简化计算, 将 F-theta 等效为一个焦距为 f 的单透镜, 激光束经过单透镜后的光线传输方向的计算公式为

$$\begin{pmatrix} r' \\ \varphi' \end{pmatrix} = \begin{pmatrix} 1 & 0 \\ -\frac{1}{f} & 1 \end{pmatrix} \begin{pmatrix} r \\ \varphi \end{pmatrix}, \quad (12)$$

计算结果可以表示为

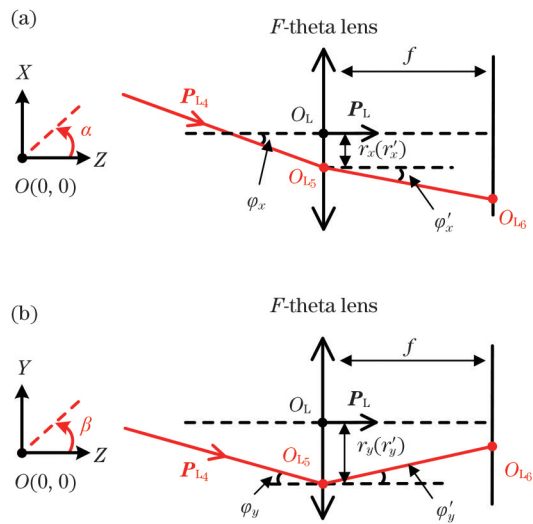


图 2 激光束投影示意图。(a)X-Z平面;(b)Y-Z平面
Fig. 2 Schematic diagrams of the laser beam projections. (a) X-Z plane; (b) Y-Z plane

$$\begin{cases} r'_x = r_x \\ \varphi'_x = -\frac{r_x}{f} + \varphi_x \\ r'_y = r_y \\ \varphi'_y = -\frac{r_y}{f} + \varphi_y \end{cases} \quad (13)$$

式(13)可以转换为聚焦激光焦点坐标(x, y)以及传输方向(α, β),即

$$\begin{cases} x = r'_x + f \tan \varphi'_x \\ \alpha = \varphi'_x \\ y = r'_y + f \tan \varphi'_y \\ \beta = \varphi'_y \end{cases} \quad (14)$$

最终,反射镜偏转角度($\theta_1, \theta_2, \theta_3, \theta_4$)和扫描激光的四轴坐标(x, y, α, β)之间的关系可以表示为

$$(\theta_1, \theta_2, \theta_3, \theta_4) = (x, y, \alpha, \beta) \begin{pmatrix} k_{11} & k_{12} & k_{13} & k_{14} \\ k_{21} & k_{22} & k_{23} & k_{24} \\ k_{31} & k_{32} & k_{33} & k_{34} \\ k_{41} & k_{42} & k_{43} & k_{44} \end{pmatrix}. \quad (15)$$

由上述推导关系可以计算得到矩阵系数 $k_{11} \sim k_{44}$ 。

双振镜激光扫描系统的工作流程为:首先根据加工需求确定四轴激光扫描路径,然后将扫描路径离散为若干个扫描点,将扫描点的坐标依次代入式(1)计算得到该点对应的反射镜偏转角度,最后将偏转角度数据依次同时传输给两个振镜执行四轴激光扫描。

3 实验材料、装置与方法

实验材料为 3.6 mm 厚玻璃纤维复合材料板,该材料由玻璃纤维和氰酸酯树脂复合而成。双振镜激光扫描加工系统示意图如图 3 所示,实验中采用的激光器的脉冲宽度为 436 fs,波长为 1030 nm。激

光出射后先经过扩束镜,再由四分之一波片将线偏振光转换为圆偏振光,以避免激光偏振态对加工过程的影响。双振镜系统中的 G_1 和 G_2 都属于一个二轴振镜(Scanlab, Basicube 14), G_3 和 G_4 都属于另一个二轴振镜(Scanlab, Intelliscan III 30),第一个振镜的出光口与第二个振镜的入光口同心,且间距为 300 mm。经过双振镜后的激光由 F-theta 镜聚焦在待加工材料表面,待加工材料放置在一个电动 Z 轴位移台上。

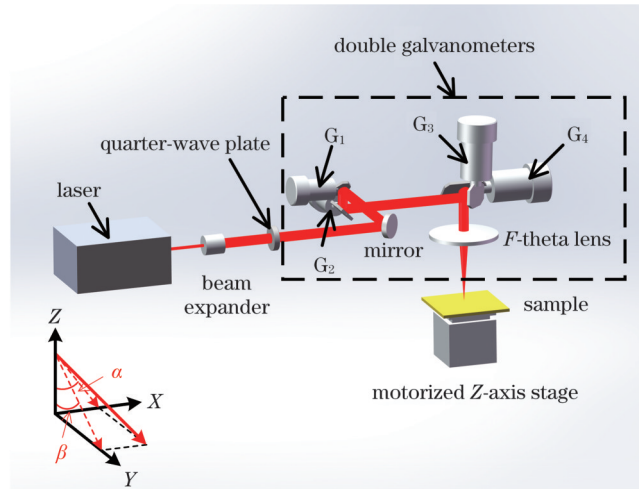


图 3 双振镜激光扫描加工系统示意图
Fig. 3 Schematic diagram of the dual galvanometer laser scanning processing system

激光制孔采用逐层扫描的加工策略,激光扫描路径如图 4 所示。在 X-Y 平面上,激光的扫描路径为同心圆,其中内圈和外圈的半径分别为 3 mm 和 5 mm,同心圆的填充间距为 15 μm,如图 4(a)所示。在 X-Z 平面上,当激光扫描内圈时,激光入射角设置为 0°,且激光入射角随扫描半径的增加而逐渐变大($\alpha_2 > \alpha_1 > 0$),以防止侧壁遮挡激光能量,如图 4(b)所示。激光去除一层材料后,电动 Z 轴位移台将待加工材料抬升,使激光焦点再次落在材料上。重复上述过程,直至材料被完全切穿。加工过程中使用的激光脉冲能量为 110 μJ,重复频率为 120 kHz,扫描速度为 500 mm/s,每次激光扫描去除的材料深度为 40 μm。加工完成后,使用体视显微镜(Stemi 508)观察孔的光学形貌,使用扫描电子显微镜(SEM, Quanta 200)观察侧壁的微观形貌,使用激光共聚焦显微镜(Keyence VK-X1000)测量侧壁的三维形貌和孔侧壁的表面粗糙度(S_a),其中表面粗糙度的测量取样区域是 1 mm × 1 mm 的矩形。

4 分析与讨论

4.1 孔侧壁锥度的形成原因

将最外圈激光入射角设置为 3°,孔入口直径符合预期,且没有观察到明显的材料碳化,如图 5(a)所示。

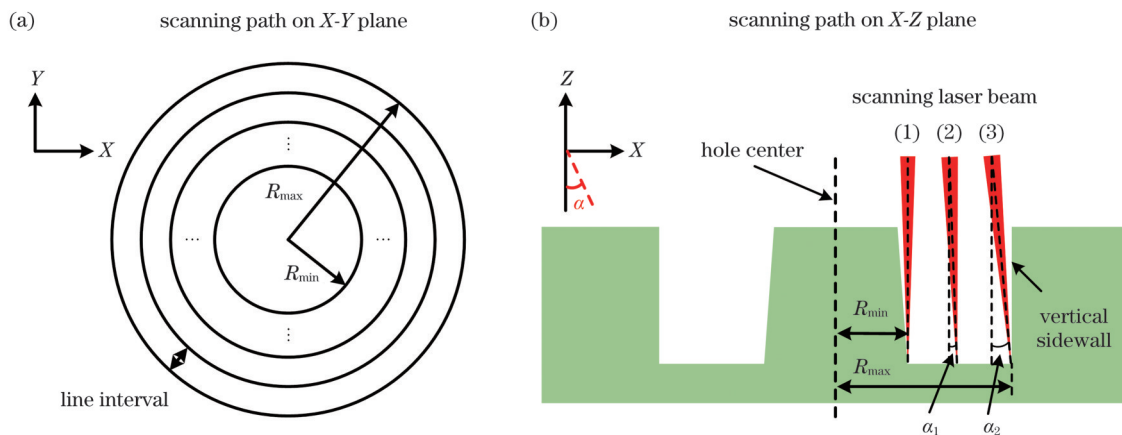


图 4 用于圆柱孔加工的双振镜激光扫描路径。(a)X-Y平面上的激光扫描路径;(b)X-Z平面上的激光扫描路径

Fig. 4 Dual galvanometer laser scanning path for cylindrical hole drilling. (a) Laser scanning path on the X-Y plane; (b) laser scanning path on the X-Z plane

然而,在孔出口处仍然存在残余材料,如图 5(b)所示。随着钻孔深度增加,残余材料逐渐积累,从而形成倾斜的侧壁。侧壁锥度形成的原因如图 5(c)所示,在相同的激光扫描次数下,扫描路径中间区域同一位置处的材料会被两侧相邻激光脉冲多次作用,而扫描路径最

内圈和最外圈处的材料仅受一侧相邻激光脉冲的作用,导致中间区域材料的加工深度较扫描边缘区域材料更大。加工进行至一半时,侧壁的三维形貌如图 5(d)所示,可见此时孔中间区域的加工深度已经明显高于两侧,侧壁的锥度已经开始积累。

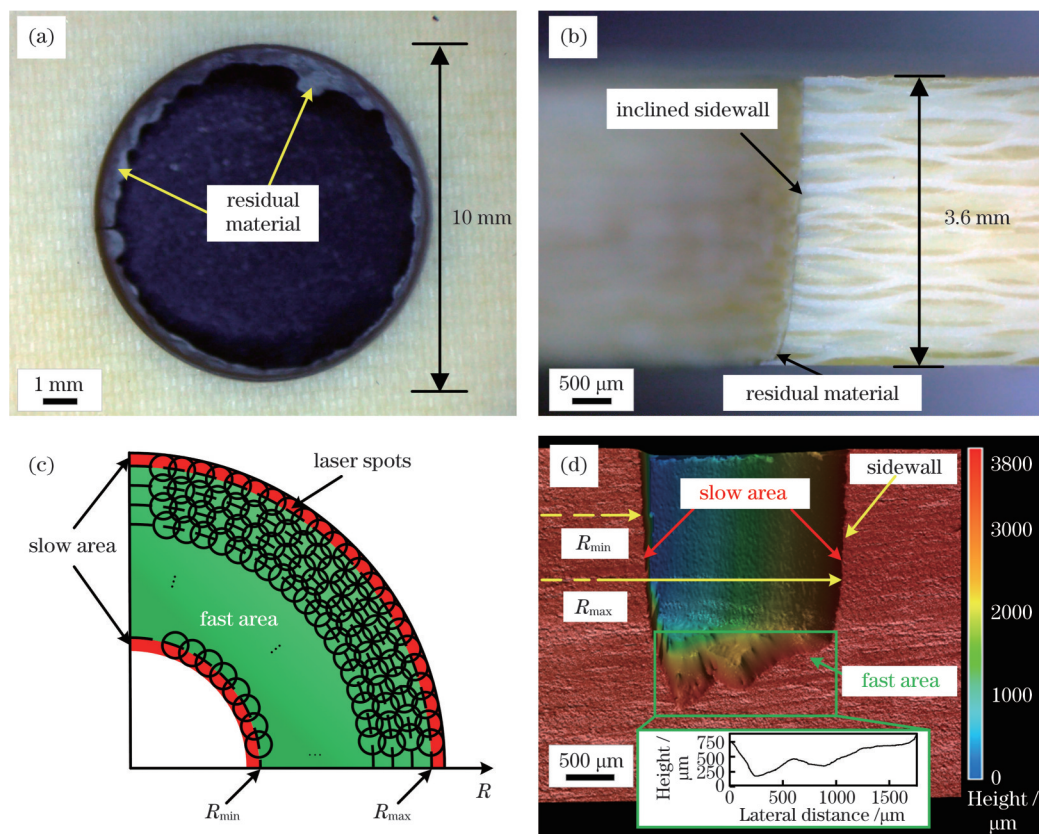


图 5 最大激光入射角为 3° 时的加工结果。(a)入口形貌;(b)侧壁形貌;(c)侧壁锥度形成示意图;(d)加工进行至一半时侧壁的三维形貌图

Fig. 5 Processing results when the max laser angle-of-incidence was 3°. (a) Entrance morphology; (b) sidewall morphology; (c) schematic diagram of sidewall taper formation; (d) three-dimensional topography of the sidewall halfway through the processing

4.2 激光入射角度对侧壁锥度的影响

激光入射角度对孔底部材料去除效率的影响如

图 6(a)所示。对于孔底部,激光入射角越大,作用在孔底部的激光光斑尺寸越大,激光能量密度越小,导致

材料的去除效率下降。图 5(d)所示的检测结果也证明了这一观点。对于孔侧壁,激光入射角的影响则恰好相反,如图 6(b)所示,激光入射角越大,作用在孔侧壁上的激光光斑尺寸越小,激光能量密度越高,从而导致材料去除效率增大。孔侧壁锥度随激光入射角变化

的实验结果如图 6(c)所示,当激光入射角从 3° 增大到 7° 时,孔侧壁锥度从 4.16° 减小到 0.65° 。实验结果表明,增加激光入射角可以增大激光对侧壁材料的去除效率,减小孔侧壁的锥度。然而在上述策略下,孔侧壁锥度仍无法被完全消除。

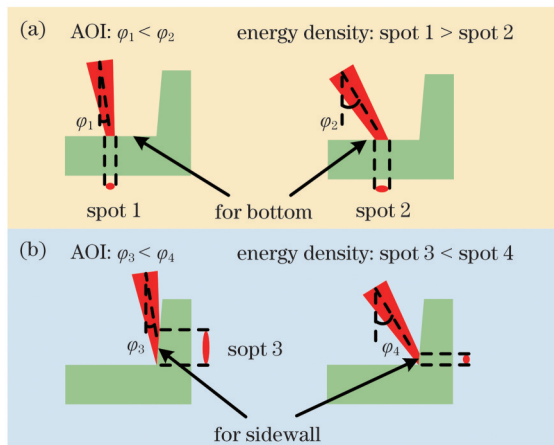


图 6 激光入射角对材料去除效率的影响。(a)激光入射角对孔底部激光能量密度影响的示意图;(b)激光入射角对孔侧壁激光能量密度影响的示意图;(c)激光入射角对孔侧壁锥度的影响

Fig. 6 Effect of laser angle-of-incidence (AOI) on the material removal efficiency. (a) Schematic diagram of the effect of laser angle-of-incidence on the laser energy density at the bottom of the hole; (b) schematic diagram of the effect of laser angle-of-incidence on the laser energy density at the sidewall of the hole; (c) effect of laser angle-of-incidence on the sidewall taper of the hole

针对以上问题,采用边缘补偿扫描方法来提高孔侧壁的材料去除率,如图 7(a)所示。加工时首先采用与上述加工方法一致的同心圆扫描,每扫描完一层材料后,激光再沿着孔的侧壁额外扫描一次,以避免侧壁

处的材料积累。实验结果如图 7(b)所示,当最外圈激光入射角为 3° 时,侧壁锥度显著下降至 0.24° ;当最外圈激光入射角增大至 4° 时,侧壁锥度为 -0.14° ;随着激光入射角继续增大,孔侧壁的负锥度也会进一步增大。

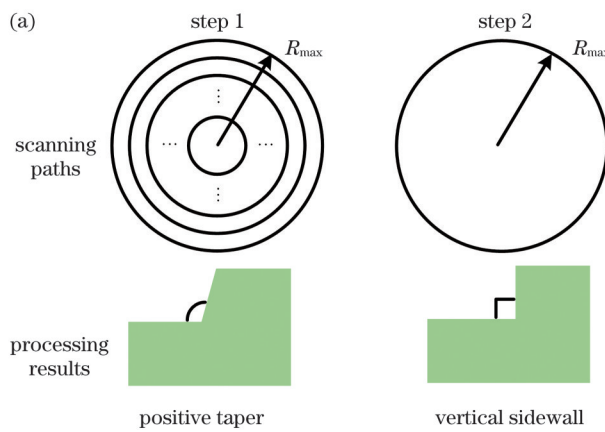


图 7 边缘补偿扫描加工法。(a)加工方法的分步示意图;(b)在边缘补偿扫描加工过程中,激光入射角对侧壁锥度的影响

4.3 直壁圆孔双振镜激光扫描制造结果分析

图 8 展示了直壁圆孔的加工结果,其中扫描路径最外圈的激光入射角设置为 3.7° 。孔入口直径为 $10 \text{ mm} \pm 10 \mu\text{m}$,如图 8(a)所示;入口热影响区宽度为 $8.79 \mu\text{m}$,如图 8(b)所示;侧壁的宏观形貌如图 8(c)所示,侧壁与材料表面完全垂直,消除了侧壁锥度;侧壁平整,表

面粗糙度(S_a)小于 $2 \mu\text{m}$,没有发现材料分层和纤维拉出等加工缺陷,如图 8(d)所示;孔出口直径为 $10 \text{ mm} \pm 10 \mu\text{m}$,如图 8(e)所示;出口热影响区宽度为 $9.08 \mu\text{m}$,如图 8(f)所示,出口形貌、加工质量与入口一致。实验结果表明,双振镜激光扫描系统可以实现玻璃纤维复合材料直壁圆孔的高精度、高质量加工。

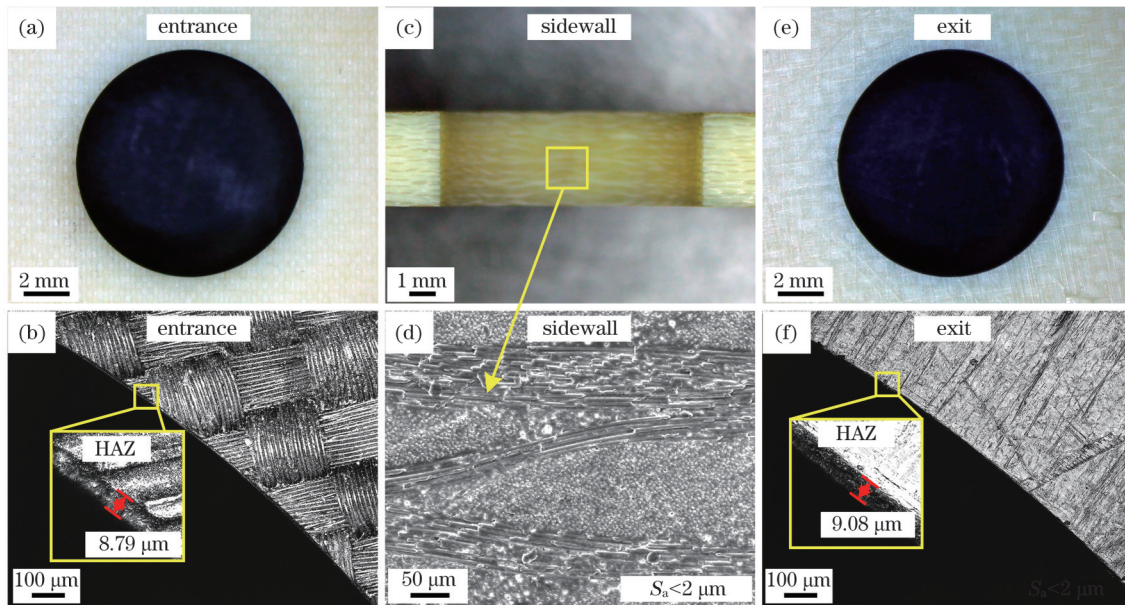


图8 直壁圆孔的加工结果。(a)入口形貌;(b)入口热影响区;(c)侧壁宏观形貌;(d)侧壁微观形貌;(e)出口形貌;(f)出口热影响区

Fig. 8 Processing results of the straight wall circular hole. (a) Entrance morphology; (b) heat-affected zone (HAZ) at the entrance; (c) macroscopic morphology of the sidewall; (d) micro morphology of the sidewall; (e) exit morphology; (f) exit HAZ

5 结 论

提出了一种双振镜激光扫描加工系统,建立了反射镜角度与激光扫描路径的数学模型,实现了激光的四轴联动扫描。基于双振镜激光扫描加工系统开展了玻璃纤维复合材料制孔实验。实验结果表明,由于激光光斑的重叠率比较低,扫描边缘的材料去除率低于扫描中间区域。增大激光入射角可以提高激光对侧壁材料的去除效率,随着激光入射角从 3° 增大到 7° ,侧壁锥度从 4.16° 减小到 0.65° 。提出了一种边缘补偿扫描方法,该方法可以进一步降低侧壁锥度,该方法结合 3.7° 激光入射角可以实现垂直侧壁的加工。加工结果表明,孔入口和出口的几何尺寸基本一致,孔直径达到 10 mm ,热影响区宽度小于 $10\text{ }\mu\text{m}$,侧壁上没有发现材料分层和纤维拔出等缺陷,侧壁表面粗糙度小于 $2\text{ }\mu\text{m}$ 。本工作提供了一种新的激光四轴扫描方法,提高了激光对玻璃纤维复合材料孔结构的制造能力和制造质量,具有较高的工业应用价值。

参 考 文 献

- [1] Bilisik K, Kaya G Y, Ozdemir H, et al. Applications of glass fibers in 3D preform composites[M]//Sgollo V M. Advances in glass science and technology. London: InTech, 2018.
- [2] Badie M A, Mahdi E, Hamouda A M S. An investigation into hybrid carbon/glass fiber reinforced epoxy composite automotive drive shaft[J]. Materials & Design, 2011, 32(3): 1485-1500.
- [3] Çelik Y H, Türkan C. Investigation of mechanical characteristics of GFRP composites produced from chopped glass fiber and application of Taguchi methods to turning operations[J]. SN Applied Sciences, 2020, 2(5): 849.
- [4] Morampudi P, Namala K K, Gajjela Y K, et al. Review on glass fiber reinforced polymer composites[J]. Materials Today: Proceedings, 2021, 43: 314-319.
- [5] Liu D F, Tang Y J, Cong W L. A review of mechanical drilling for composite laminates[J]. Composite Structures, 2012, 94(4): 1265-1279.
- [6] Kavad B V, Pandey A B, Tadavi M V, et al. A review paper on effects of drilling on glass fiber reinforced plastic[J]. Procedia Technology, 2014, 14: 457-464.
- [7] Demirsöz R, Yaşar N, Korkmaz M E, et al. Evaluation of the mechanical properties and drilling of glass bead/fiber-reinforced polyamide 66 (PA66)-based hybrid polymer composites[J]. Materials, 2022, 15(8): 2765.
- [8] Domingo R, de Agustina B, Ayllón J. Study of drilled holes after a cryogenic machining in glass fiber-reinforced composites[J]. Applied Sciences, 2022, 12(20): 10275.
- [9] Deepak D, Ashwin Pai K. Study on abrasive water jet drilling for graphite filled glass/epoxy laminates[J]. Journal of Mechanical Engineering and Sciences, 2019, 13(2): 5126-5136.
- [10] Kumar G, Rangappa S M, Siengchin S, et al. A review of recent advancements in drilling of fiber-reinforced polymer composites[J]. Composites Part C: Open Access, 2022, 9: 100312.
- [11] Chaichanawong J, Thongchuea C, Areerat S. Effect of moisture on the mechanical properties of glass fiber reinforced polyamide composites[J]. Advanced Powder Technology, 2016, 27(3): 898-902.
- [12] Nuryanta M I, Sentanuhady J, Muflikhun M A. Moisture absorption behavior of hybrid composite laminates consist of natural and glass fiber[J]. Materials Today: Proceedings, 2022, 66: 2924-2928.
- [13] Padmanabham G, Bathe R. Laser materials processing for industrial applications[J]. Proceedings of the National Academy of Sciences, India Section A: Physical Sciences, 2018, 88(3): 359-374.
- [14] Miyamoto Y. Direct treatment of interaction between laser-field and electrons for simulating laser processing of metals[J]. Scientific Reports, 2021, 11: 14626.
- [15] Tamrin K F, Sheikh N A, Sapuan S M. Laser drilling of composite material: a review[M]//Abdullah A B, Sapuan S M. Hole-making and drilling technology for composites. Amsterdam: Elsevier, 2019: 89-100.
- [16] Bhaskar V, Kumar D, Singh K K. Laser processing of glass fiber reinforced composite material: a review[J]. Australian Journal of Mechanical Engineering, 2019, 17(2): 95-108.

- [17] Nath A K. Laser drilling of metallic and nonmetallic substrates [M]//Hashmi S. Comprehensive materials processing. Amsterdam: Elsevier, 2014: 115-175.
- [18] Pattanayak S, Panda S. Laser beam micro drilling: a review[J]. Lasers in Manufacturing and Materials Processing, 2018, 5(4): 366-394.
- [19] McNally C A, Folkes J, Pashby I R. Laser drilling of cooling holes in aeroengines: state of the art and future challenges[J]. Materials Science and Technology, 2004, 20(7): 805-813.
- [20] Fan Z J, Sun X M, Mei X S, et al. Enhanced molten salt resistance by sidewall pores repair during fs laser drilling of a thermal barrier-coated superalloy[J]. Materials, 2019, 12(12): 1905.
- [21] Wang M L, Yang L J, Zhang S, et al. Experimental investigation on the spiral trepanning of K24 superalloy with femtosecond laser [J]. Optics & Laser Technology, 2018, 101: 284-290.
- [22] Sun X M, Dong X, Wang K D, et al. Experimental investigation on thermal effects in picosecond laser drilling of thermal barrier coated In718[J]. Optics & Laser Technology, 2019, 113: 150-158.
- [23] Yan Y Z, Ji L F, Bao Y, et al. An experimental and numerical study on laser percussion drilling of thick-section alumina[J]. Journal of Materials Processing Technology, 2012, 212(6): 1257-1270.
- [24] Tao N R, Chen G Y, Yu T Y, et al. Dual-beam laser drilling process for thick carbon fiber reinforced plastic composites plates [J]. Journal of Materials Processing Technology, 2020, 281: 116590.
- [25] Chao H, Malte W, Arnold G. Recast-free helical drilling of fused silica using SHG picosecond laser pulses[J]. Journal of Laser Micro, 2020, 15(2):158-163.
- [26] Jahns D, Kaszemeikat T, Mueller N, et al. Laser trepanning of stainless steel[J]. Physics Procedia, 2013, 41: 630-635.
- [27] Uchtmann H, He C, Gillner A. High precision and high aspect ratio laser drilling: challenges and solutions[J]. Proceedings of SPIE, 2016, 9741: 974106.
- [28] Jiwhan N, Jaehoon L, Jeong S, et al. Trepanning optical system using tilting focus lens for laser drilling process[J]. Journal of Laser Micro, 2009, 4(3): 239-244.
- [29] Romoli L, Vallini R. Experimental study on the development of a micro-drilling cycle using ultrashort laser pulses[J]. Optics and Lasers in Engineering, 2016, 78: 121-131.
- [30] Zhu Q C, Fan P X, Li N, et al. Femtosecond-laser sharp shaping of millimeter-scale geometries with vertical sidewalls[J]. International Journal of Extreme Manufacturing, 2021, 3(4): 045001.
- [31] Sonner C, Rabe M. Scanning head with integrated beam position sensor and adjustment arrangement for an off-line adjustment: US20180169788[P]. 2018-06-21.
- [32] Martin H, Dmitry B, Markus G. Scan head as part of a laser drilling and cutting device: EP 1656234B1[P]. 2007-07-17.

Drilling Straight-Walled Holes in Glass Fiber-Reinforced Composites by Double Galvanometer Laser Scanning

Zhang Pin³, Qiao Yaqing^{1*}, Su Xiaohui¹, Gao Hui^{1,2}, Xiong Wei^{1,2}, Deng Leimin^{1,2}

¹Wuhan National Laboratory of Optoelectronics, Huazhong University of Science and Technology, Wuhan 430074, Hubei, China;

²Optical Valley Laboratory, Wuhan 430074, Hubei, China;

³Aviation Key Lab of Science and Technology on High Performance Electromagnetic Windows, AVIC Research Institute for Special Structures of Aeronautical Composite, Jinan 250023, Shandong, China

Abstract

Objective Glass fiber-reinforced composite plates (GFRP) possess several advantageous properties, such as wear resistance, corrosion resistance, a high strength-to-weight ratio, and high fracture toughness. Hence, they have found extensive applications in the aviation, automotive, shipbuilding, and chemical industries. However, the distinctive structure of GFRP results in significant challenges during drilling processes, particularly when aiming for high-quality holes. Mechanical and water jet drilling methods often introduce defects, such as delamination and fiber pull-out. Hence, laser processing has emerged as a viable alternative. It eliminates the interaction forces between the laser and material owing to being a noncontact method, effectively avoiding the aforementioned defects. Consequently, it has proven to be an effective method for drilling GFRP. However, laser punching drilling and two-axis laser scanning drilling suffer from limited laser control flexibility and difficulties in eliminating sidewall tapering. Moreover, laser punching drilling is only suitable for processing small circular holes. Although laser rotary cutting and five-axis laser drilling can adjust the laser angle-of-incidence and eliminate sidewall taper, their maximum processing diameter does not exceed 5 mm, limiting the drilling of larger holes. This study proposes a four-axis laser scanning processing technique based on a dual galvanometer system. The proposed technique successfully eliminates sidewall tapering and expands the range of hole diameters that can be processed.

Methods This study used two galvanometers to construct a four-axis laser scanning system, enabling four-axis laser scanning through a correspondence between the four-axis coordinates of the laser focus and deflection angles of the galvanometer mirrors. The experimental material was a 3.6 mm thick GFRP. The laser employed in the experiment had a pulse width and wavelength of 436 fs and 1030 nm, respectively. Following its passage through the four-axis laser-scanning system, the laser was focused onto the workpiece surface using an *F*-theta lens. The GFRP specimen was placed on an electric *Z*-axis stage. Laser drilling was performed using a layer-by-layer scanning approach, where the scanning path of the laser in the *X-Y* plane consisted of concentric circles. Additionally, the laser angle-of-incidence gradually increased with the scanning radius to prevent the sidewall from obstructing the laser energy. After removing each material layer, the electric *Z*-axis elevated the workpiece, aligning the laser focus with the next

layer. This iterative process continued until the desired drilling depth was achieved. Subsequently, the optical morphology of the drilled holes was examined using a stereomicroscope. The microstructure of the sidewall was analyzed using a scanning electron microscope. Furthermore, the 3D morphology and surface roughness (S_a) of the sidewall were measured using laser confocal microscopy. The roughness measurement encompassed a rectangular sampling area of $1\text{ mm} \times 1\text{ mm}$.

Results and Discussions The low laser pulse overlap rate at the sidewall affects the material removal rate, resulting in the accumulation of sidewall taper. Several improvements are observed by gradually increasing the laser angle-of-incidence from 3° to 7° . First, the laser spot size at the sidewall reduces, increasing laser energy density. Consequently, the sidewall taper decreases from 4.16° to 0.65° . However, increasing the laser angle-of-incidence does not eliminate sidewall tapering. The edge compensation scanning method can further enhance the material removal rate at the sidewall, ultimately eliminating the sidewall taper. Application of the method significantly decreases the sidewall taper to 0.24° at the laser angle-of-incidence of 3° . Similarly, the sidewall tapering reaches -0.14° at the laser angle-of-incidence of 4° . The aforementioned results are considered to successfully fabricate a circular hole with a diameter of up to 10 mm on a 3.6 mm thick GFRP specimen. Notably, the width of the heat-affected zone at the entrance and exit of the hole is less than $10\text{ }\mu\text{m}$. Additionally, the hole sidewall exhibits a smooth surface with a surface roughness of less than $2\text{ }\mu\text{m}$.

Conclusions This study proposes a dual-galvanometer laser scanning processing system and develops a mathematical model to establish the relationship between mirror angles and laser scanning paths, enabling four-axis coordinated laser scanning. Laser-drilling GFRG experiments are conducted using a dual-galvanometer laser scanning processing system. The results show that the material removal rate at the scanning edges is lower than that at the central region owing to the weak overlap of the laser spots. Increasing the laser incident angle can improve the material removal efficiency at the sidewalls and reduce the sidewall taper. An edge-compensation scanning method is proposed to reduce sidewall taper. A vertical sidewall is processed at a laser angle-of-incidence of 3.7° . The processing results demonstrate consistent geometric dimensions at the entrance and exit of holes. Specifically, the hole diameter is measured to be 10 mm, and the width of the heat-affected zone is less than $10\text{ }\mu\text{m}$. Moreover, sidewalls do not have defects, such as material delamination and fiber pull-out. Furthermore, the sidewall roughness is less than $2\text{ }\mu\text{m}$. This study proposes a novel four-axis laser scanning method that enhances the manufacturing capability and quality of holes in GFRP, offering substantial potential for valuable industrial applications.

Key words laser technique; laser drilling; four-axis laser scanning; glass fiber-reinforced composites; femtosecond laser